RSC Applied Polymers

ROYAL SOCIETY OF CHEMISTRY

PAPER

View Article Online
View Journal

Cite this: DOI: 10.1039/d6lp00122j

Mechanical properties of individual conductive protein nanowires and their percolation behavior in elastomer nanocomposites

Eric Chia,[a] Jayesh M. Sonawane,[b] Trevor L. Woodard,[c] Meng-Chen Chiang,[d] Jessica D. Schiffman[d,e] and Stephen S. Nonnenmann[*a,e]

High-performance soft electronics require conductive fillers that balance functional electrical properties with mechanical compliance. This study investigates conductive protein nanowires (CPNs) from *Geobacter sulfurreducens* as a sustainable, mechanically compliant alternative filler in polydimethylsiloxane (PDMS)-based nanocomposites. The primary objective was to establish the fundamental mechanics of individual CPNs and characterize their integration into hydrophobic elastomers. Local nanomechanical characterization established the first experimental elastic modulus for individual CPNs at 1.3 ± 0.1 GPa, validating their potential as compliant components compared to significantly stiffer synthetic alternatives. As incorporated into the archetype elastomer PDMS, nanocomposites were measured using amplitude modulation–frequency modulation bimodal imaging as a function of filler loading (wt%), revealing a rheological percolation threshold of 0.8 wt% and tunable stiffness in the low-MPa range. Additional electrical transport measurements as a function of filler loading yielded an electrical percolation threshold of 6.7 wt% for CPN/PDMS. Template fabrication of CPN/PDMS using anodic aluminum oxide (AAO) successfully lowered the electrical threshold to 0.1 wt% and demonstrated enhanced conductance in nanocomposites with nanochannel texturing. Overall, CPN/PDMS nanocomposites exhibit tunable moduli, electrical conductivity, and percolation thresholds that are further reduced by nanostructured geometric confinement templating to enable an effective soft electronics materials platform.

Received 8th April 2026,
Accepted 25th May 2026

DOI: 10.1039/d6lp00122j

rsc.li/rscapplpolym

1 Introduction

High-performance soft electronics are critical for use in bioelectronics,[1,2] personalized healthcare monitoring,[3–5] and soft robotics applications.[6,7] A primary challenge in this field is balancing functional electrical properties with mechanical compliance.[8–11] Conventional approaches typically involve infiltrating elastomeric matrices, such as polydimethylsiloxane (PDMS), with conductive nanowires/nanotubes due to their high conductivity and aspect ratios. Unfortunately, high loadings of these nanotubes (*e.g.* gold (Au),[12,13] silver (Ag),[14,15] copper (Cu)[16] or carbon nanotube (CNT)[17]) have been shown to reduce elasticity dramatically with increased loading. For example, CNT composites have a narrow mechanical tuning range (between 0.12–0.5 wt%), which causes the material to experience an increase in storage modulus, and limits its processability for highly compliant applications.[9] While it is certainly possible to process CNTs at much higher mass loadings, doing so induces severe embrittlement; thus, the rapid stiffening observed at very low loadings severely narrows the effective mechanical tuning window for soft electronics applications. Furthermore, silver nanowires (AgNWs) are prone to surface oxidation which degrades interfacial adhesion.[18,19] Liquid metal alternatives, though flexible, also suffer from oxidation issues and require complex fabrication processes.[20–22]

Conductive protein nanowires (CPNs), derived from the naturally expressed electrically conductive type IV pili (e-pili)[7,11] of *Geobacter sulfurreducens* (*G. sulfurreducens*), produce nanowires from peptide subunits.[23] Harvesting "wild type" e-pili usually requires maintaining challenging, anaerobic conditions. However recent progress demonstrated that CPNs could be successfully isolated from a diverse array of microorganisms under aerobic conditions,[24–26] generating higher quantities sufficient for exploration as a nanocomposite filler. Consequently, the scope of CPN applications has expanded to include the development of effective CPN-enabled

[a]*Department of Mechanical and Industrial Engineering, University of Massachusetts Amherst, 686 N Pleasant St, Amherst, MA 01003, USA. E-mail: ssn@umass.edu*
[b]*Department of Microbiology, Central University of Rajasthan, Ajmer 305817, Rajasthan, India*
[c]*Department of Microbiology, University of Massachusetts Amherst, 639 N Pleasant St, Amherst, MA 01003, USA*
[d]*Department of Chemical and Biomolecular Engineering, University of Massachusetts Amherst, 240 Thatcher Rd, Amherst, MA 01003, USA*
[e]*Material Science and Engineering Graduate Program, University of Massachusetts Amherst, Amherst, Massachusetts 01003-9303, USA*

electronic devices, such as memristors,[27] ammonia sensors,[28] and power generators.[29]

Despite the success realized in CPN-based electronics, the mechanical properties of CPNs remain largely underexplored. While molecular dynamics simulations suggest an elastic modulus between 0.4 GPa[30] and 0.8 GPa[31], an absence of experimental validation *via* force-based measurements of individual CPNs limits the current understanding. Initial studies demonstrated polymer nanocomposites comprising CPNs dispersed in polyvinyl alcohol (PVA) exhibited appreciable conductivity ($\sim 10^{-7}$ S cm^{-1}, 0.2 wt%).[32] However, no reports on the effects of CPN integration into PVA on the resulting modulus were made.

In this study, CPNs are introduced as a biologically derived, intrinsically conductive nanofiller that provides moderate mechanical reinforcement while bestowing an electrical pathway, as incorporated into an elastomeric PDMS matrix. Using scanning probe nanomechanics methods, the first force-based experimental modulus value for individual CPNs is established, bridging a critical gap for rational polymer nanocomposite design. Despite advances in the aerobic production of CPNs to yield higher quantities sufficient for fabricating polymer nanocomposite test structures, the sample volumes remain limited to nominally 10–20 μL, which poses experimental challenges for measuring the functional properties of CPN/PDMS polymer nanocomposites, as conventional tensile testing or transport measurements will not provide adequate sensitivity or resolution. Here, using a combination of bimodal atomic force microscopy (AFM) imaging and electrical transport measurements, as-fabricated CPN/PDMS polymer nanocomposites of various filler loadings are shown to exhibit percolation behavior, and the resulting rheological and electrical percolation thresholds are analyzed and established. Subsequently, whole cell infiltration and anodic aluminum oxide (AAO) templating are explored to further tune electrical conduction and threshold behavior in the functional nanocomposites. The study concludes with the demonstration of a CPN/PDMS-based strain gauge, highlighting the potential of these materials for advanced sensing applications. Overall, the overarching motivation of this work is to introduce an intrinsically conductive biomaterial filler that mitigates the severe embrittlement typically caused by rigid synthetic nanomaterials, effectively balancing functional conductivity with the necessary mechanical compliance for soft devices.

2 Materials and methods

2.1 Preparation of CPNs

Escherichia coli (*E. coli*) with the expression of *G. sulfurreducens* gene cultures were routinely maintained aerobically at 30 °C in Luria–Bertani (LB) medium. For CPN production, cells were mass-cultured following the standard protocol:[33,34] they were incubated for 48 h at 30 °C on M9 agar plates supplemented with 0.5% glycerol as the carbon source, 0.5 mM Isopropyl β-D-1-thiogalactopyranoside (IPTG) to induce pilin expression, and 50 μg mL^{-1} kanamycin. After incubation, cells were scraped from the agar, resuspended in M9 medium, and pelleted by centrifugation. The cell pellets were then resuspended in 50 mL of 150 mM ethanolamine buffer (pH 10.5) for protein nanowire isolation *via* ammonium sulfate precipitation. Purified CPN preparations were dialyzed repeatedly against deionized water, concentrated to 2 mL in deionized (DI) water, and stored at 4 °C until use.

2.2 Transmission electron microscopy (TEM) for CPN imaging

For TEM imaging, pili were drop-cast for 10 min on a plasma-sterilized 400 mesh copper grid coated with an ultrathin carbon film. Excess liquid was wicked off and the grid stained with 3 μL of 2% uranyl acetate for 30 s before the liquid was wicked off and grid air dried overnight. The sample was imaged on a Tecnai T12 (FEI) at 120 kV, with a spot size of 3 and camera exposure of 200 ms.

2.3 Atomic force microscopy (AFM) for nanomechanics assessment

2.3.1 Fast force mapping on a single CPN. The CPNs were harvested from *E. coli* and initially stored in DI water according to the previously published protocol mentioned.[28] The CPN solution was drop-cast on different silicon (Si), platinum-coated silicon (Pt-Si), and highly ordered pyrolytic graphite (HOPG), with 50 μL of solution sitting for 10 min and then wicked dry. Each substrate had six to eight CPNs measured using AFM by fast force mapping (FFM) (Cypher ES, Asylum Research, Oxford Instruments, Santa Barbara, CA, USA). The medium-soft tip was utilized to perform single CPN measurements (AC240TS-R3, Al-coated, spring constant = 2 N m^{-1}, resonance frequency = 70 kHz, tip radius = 7 nm).

2.3.2 Amplitude-modulated, frequency-modulated (AM–FM) AFM. For bimodal AM–FM, the same tip model was utilized. To excite the cantilever precisely with superimposed natural frequencies, photothermal excitation (blueDrive, Cypher ES, Asylum Research, Oxford Instruments, Santa Barbara, CA, USA) is utilized to drive the cantilever of AFM probe rather than conventional piezoelectric excitation that possess complicated coupling of mechanical responses for signal processing.[35]

2.4 CPN/PDMS and *E.coli*/PDMS nanocomposites fabrication

The weight percentage (wt%) of CPNs was calculated by using eqn (1):

$$\frac{w_{\mathrm{CPNs}}}{w_{\mathrm{base}} + w_{\mathrm{curing\ agent}} + w_{\mathrm{CPNs}}} \times 100\% \quad (1)$$

where w_{CPNs} is the weight of CPNs, w_{base} is the weight of PDMS base, $w_{\mathrm{curing\ agent}}$ is the weight of PDMS curing agent. CPNs in DI water were first evaporated under vacuum (0.01 torr, 70 °C). The dried CPNs were resuspended in a 10 : 1 (base : curing agent) PDMS solution (Sylgard 184, Dow), vortexed (model SI-0246, MRC, 15 s), and ultrasonicated (model M2800H,

Branson, 15 min). This mixing cycle was repeated three times to disperse the CPNs.

The CPN/PDMS mixture was spin-coated (3000 rpm, 2 min) onto silicon wafers and cured at 60 °C for 16 h. Samples with filler loadings of 1, 2, 5, and 10 wt% were prepared. For dispersion verification, CPNs were tagged with fluorescein isothiocyanate (FITC) (1 mg mL^{-1}), dialyzed to remove excess dye, and imaged *via* fluorescence microscopy. To verify the dispersion of CPNs in PDMS, the CPNs were tagged with fluorescein isothiocyanate (FITC). The CPNs with 10 wt% in DI water were tagged with 10 μL of 1 mg mL^{-1} FITC and stored in the refrigerator overnight. The solution was then dialyzed to remove the excess FITC and the fabrication steps were repeated to have 10 wt% FITC tagged-CPN/PDMS. The fluorescence images were taken by Zeiss Axio Imager A2M, with an excitation wavelength of 488 nm. The *E. coli*/PDMS solution was also prepared using the same steps with 5, 10, 15, and 20 wt% of *E. coli* to PDMS according to previous work.[28]

2.5 Electrical conductivity measurements & analysis

The prepared CPN/PDMS solution was drop-cast on interdigitated electrode with 0.5 mm gap length, before being baked in the furnace with 60 °C for 16 h. This sample was used for conductivity test with respect to CPN weight percentage to PDMS solution. Duplicate samples of 6, 7, 8, 20, and 24 wt%, and one sample of 10 and 16 wt% were fabricated to study the effects of CPN loading on conductivity. CPN/PDMS solutions (10 μL) were drop-cast on the interdigitated electrode and the *I–V* curves were measured by Keithley 2401 using 2-points probe method with 0.2 V bias applied. The conductivity, σ was calculated using eqn (2):

$$\sigma = \frac{I}{V}\frac{L}{ntw} \tag{2}$$

where the I and V are measured current and applied voltage, respectively, that could be readily extracted from *I–V* curves, L is the distance between electrodes, w is the width of a single electrode, and n is the number of electrode pairs. The geometry of the interdigitated electrodes is L = 0.5 mm, w = 4 mm, and n = 10 pairs. Also, t is the thickness of the film that is approximately 0.25 mm.

2.6 Nanochannel-templated CPN/PDMS nanocomposites

To improve geometrical confinement, CPN solutions (0.5, 1, and 3 wt%) were infiltrated into AAO templates (140 nm pore diameter, DP450-140S-50000, Topmembranes Technology) *via* ultrasonication and drying. The CPN-filled AAO templates were placed on PDMS, vacuum infiltrated (0.1 torr, 8 h), and cured. The composite was detached and sputtered with platinum for electrical testing.[36]

2.7 Dog-bone fabrication for pilot study of strain gauge application

A pilot study was conducted to evaluate the sensing potential of CPN/PDMS nanocomposites using a 20 wt% CPN loading to ensure sufficient conductivity. Dog-bone specimens were fabricated following a miniaturized ASTM-D412 standard (scaled to one-fifth of the standard length) with a thickness of 1 mm, using the mixing and curing protocols described in Section 2.3. Electrical connections were established by interfacing wires with silver paste, and resistance changes under load were recorded using a Keithley 2401 source meter.

3 Results and discussion

3.1 Nanomechanics of individual CPN

Morphological analysis *via* transmission electron microscopy (TEM) and AFM confirmed that harvested CPNs possess lengths of several microns and diameters of approximately 3 nm. Fig. 1 shows the morphology of CPNs harvested from *E. coli*. The morphology of CPNs was observed using both TEM (Fig. 1a) and AFM (Fig. 1b), showing that the CPNs display nominal lengths of several microns and diameters approximately 3 nm, which is consistent with previous studies.[33,34]

AFM leverages highly sensitive tip–sample interactions in the z-dimension (approach/retract) to simultaneously image topography and measure mechanical properties across a wide dynamic range (100 Pa–100 GPa) with nanoscale spatial resolution.[37–39] FFM is capable of quickly producing high resolution 256 × 256 pixel maps of force–distance curves. To bridge the gap in mechanical data, FFM was utilized to measure the transverse elastic modulus of individual nanowires. Force–distance curves were analyzed using the loading slope[40] (Fig. 2a, red). The unloading curve exhibited significant hysteresis, indicative of viscoelastic behavior. Consequently, the elastic modulus was derived from the loading curve using the Sneddon model, assuming a Poisson's ratio of 0.5 using Eqn (3):[40]

$$\frac{dF_N}{d\delta} = \frac{16}{3\pi}E_{CPN}\delta(\cot\alpha)^{-1} \tag{3}$$

where dF_N is the loading slope, E_{CPN} is the Young's modulus of CPNs, δ is the indentation depth, and α is the half-angle of the AFM tip. A statistical analysis of measurements across mul-

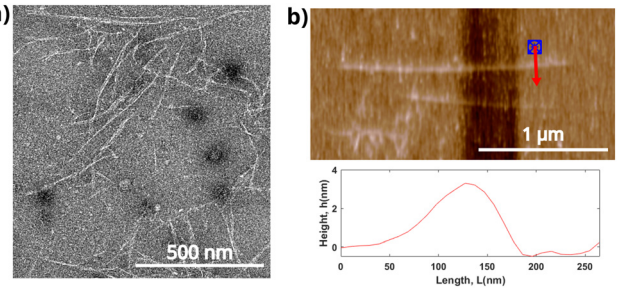

Fig. 1 Micrographs of CPN morphology. (a) A TEM image of CPNs harvested from *E. coli* modified with *G. sulfurreducens* gene expression. The nanowire lengths ranged from a few hundred nm to several micrometers in length. (b) The AFM topography of a single CPN that confirms a diameter of 3 nm.

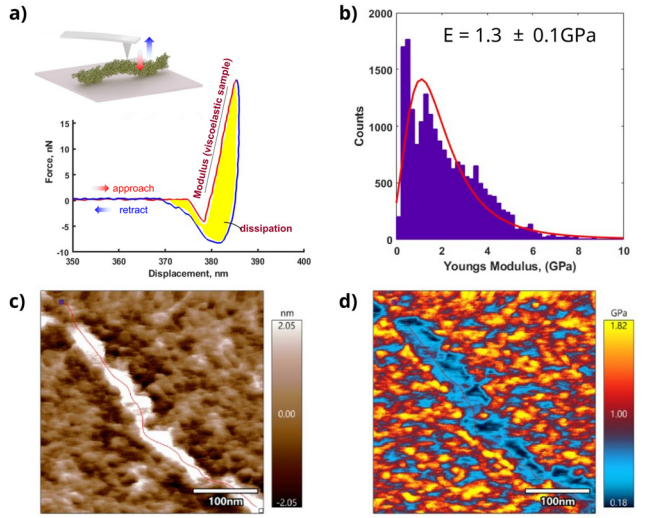

Fig. 2 Experimental details of individual CPN nanomechanics measurements *via* fast force mapping (FFM). (a) Schematic illustration of the force–distance response collected from an individual CPN. The force–distance curves are represented within each pixel in the image maps for both height and Young's modulus. (b) Shows the generalized extreme value (GEV) distribution of CPN Young's modulus on silicon (8 samples), highly-ordered pyrolytic graphite (6 samples), and platinum-coated silicon (6 samples) substrates and yield 1.3 ± 0.1 GPa. (c) Shows the height of a single CPN, which is 3 nm.[33,43] (d) Shows the corresponding Young's modulus retrieved from the force–distance curve. A curve is depicted along the CPN (red curve) to show the measured height and Young's modulus along the CPN.

tiple substrates (Si, Pt-Si, HOPG) yielded an average Young's modulus of 1.3 ± 0.1 GPa (Fig. 2b). Representative height and Young's modulus profiles extracted along a single CPN are provided in Fig. S1. This represents the first direct force-based measurement of CPN stiffness, agreeing well with previous molecular dynamics predictions (0.8 GPa).[31] Notably, this modulus is orders of magnitude lower than CNTs (1 TPa)[41] or AgNWs (90 GPa),[42] highlighting the potential of CPNs as mechanically compliant fillers.

3.2 Rheological percolation of CPN/PDMS

To assess mechanical reinforcement, AM–FM bimodal imaging was performed on CPN/PDMS composites. AM–FM bimodal AFM is an effective technique for nanomechanical measurements of small volume samples.[44] The principle behind this method is that driving the cantilever simultaneously at its first and second resonance frequencies enables the extraction of topographic and nanomechanical information within a single scan. The AM operates in first eigenmode and FM operates in second eigenmode are linearly convoluted by the means of superposition, and the response from the materials' surface through photodetector is then deconvoluted into height and loss tangent for AM portion, as well as Young's modulus and energy dissipation for FM portion accordingly.

Fabricating composites with hydrophilic CPNs and hydrophobic PDMS requires specific processing to manage phase separation. Thus, fluorescence imaging was used to confirm

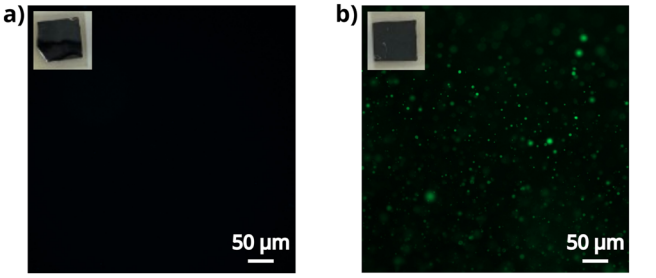

Fig. 3 Fluorescent micrographs of fluorescein isothiocyanate (FITC)-tagged CPNs verify their dispersion in PDMS composites. (a) Control PDMS-only gel lacks fluorescence, whereas the (b) 10 wt% CPN/PDMS indicate that CPNs are well dispersed as visualized by the green fluorescence. Insets in a and b are images of the samples (5 mm × 5 mm) used for fluorescence microscopy.

that FITC-tagged CPNs achieved decent dispersion within the matrix without gross phase separation. Consistent with previous work, ultrasonication was employed to mechanically disrupt aggregates; however, CPNs are expected to form bundles rather than fully exfoliate in organic solvents due to polarity differences.[45] Fig. 3a shows pristine PDMS exhibiting no fluorescence signal, confirming the absence of matrix background. Fig. 3b shows the 10 wt% CPN/PDMS nanocomposite, in which a distributed FITC signal is observed throughout the matrix without evidence of gross agglomeration, indicating effective CPN dispersion. As filler loading increased from 0 to 10 wt%, the nanocomposite elastic modulus rose from 2 MPa to 5 MPa (Fig. 4a). The AM-FM Young's modulus maps as a function of CPN loading are shown in Fig. S2. The resulting curve was fitted with a power–law relationship to determine the rheological percolation threshold, as defined by eqn (4):[9]

$$E = E_0(w - w_{cr,E})^{\beta_E} \quad (4)$$

where E is the Young's modulus, E_0 is the scaling constant for the rheological percolation curve, w is the weight percentage of infused CPNs, $w_{cr,E}$ is the weight percentage for the rheological threshold, and β_E is the exponent. The power law fit yielded a rheological CPN loading threshold of 0.8 wt%. This indicates that CPNs effectively interact with polymer chains to form a stress-transferring network at relatively low concentrations.

3.3 Electrical percolation of CPN/PDMS

While pure PDMS is a well-known electrical insulator, incorporation of conductive nanofillers like CNT,[14] graphene,[46] and AgNWs[47] beyond a critical electrical percolation threshold concentration has been shown to establish a continuous conductive pathway for electron transport.[9,10] To observe the electrical percolation behavior in CPN/PDMS nanocomposites, samples were deposited on interdigitated electrodes to measure the current–voltage response and calculate the corresponding conductivity values (see Sect. 2.4), which were then plotted as a function of CPN filler loading (7, 8, 10, 16, 20, and 24 wt%, Fig. 4b). Representative *I–V* curves above and below the electrical percolation threshold are provided in Fig. S3. The electrical

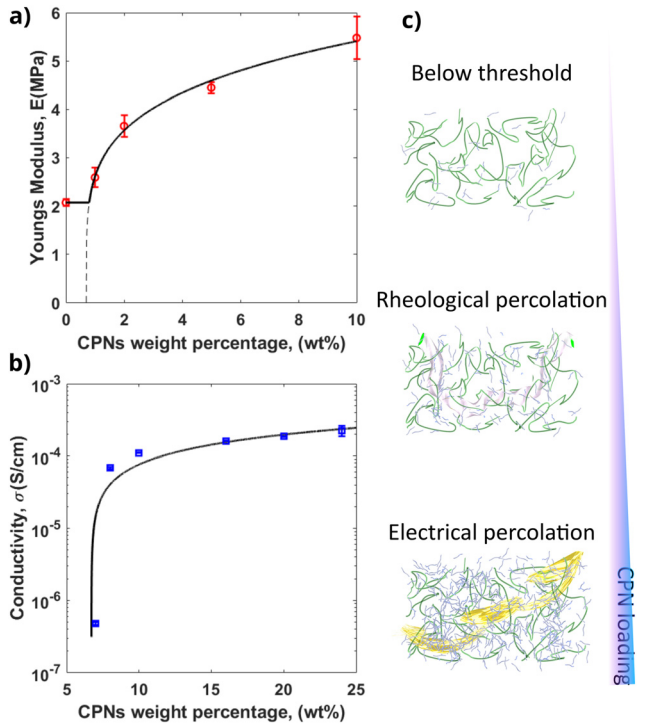

Fig. 4 Plots of (a) Young's modulus (MPa) and (b) electrical conductivity (S cm^{-1}) *vs.* filler loading (wt%). A power–law fit yields a rheological percolation threshold for CPN/PDMS of $w_{cr,E}$ = 0.8 wt% (R^2 = 0.99) in (a), while in (b) a power–law fit yields an electrical percolation threshold for CPN/PDMS of $w_{cr,\sigma}$ = 6.7 wt% (R^2 = 0.92). (c) Illustrations of the threshold evolution describing CPN–PDMS interactions.

percolation behavior is also described by a power–law relationship provided in eqn (5):[48]

$$\sigma = \sigma_0 (w - w_{cr,\sigma})^{\beta_\sigma} \quad (5)$$

where σ is the conductivity, σ_0 is the scaling constant for electrical curve, w is the weight percentage of CPN fillers, $w_{cr,\sigma}$ is the critical weight percentage that initiates electrical percolation, and β_σ is the exponent for electrical percolation. The fit yielded a critical electrical percolation threshold for CPN/PDMS of 6.7 wt% (Fig. 4b).

The observed percolation behavior is comparable to previous microbial-based CPN filler/PVA nanocomposites,[32] as well as other conventional polymer nanocomposite systems.[9,10] Below the rheological threshold, CPN interactions with PDMS chains are insufficient to support appreciable loads. As the CPN loading increases to the 0.8 wt% threshold, the CPN–PDMS interactions are sufficient to convey forces. The highly insulating PDMS matrix limits electron conduction to only between CPNs; thus, the electrical threshold increases sharply to 6.7 wt%. Classic percolation models predict that electrical percolation typically requires a higher weight percentage of nanofillers than the rheological percolation threshold, as they must form a dense, interconnected conductive network to facilitate electron transport (Fig. 4c). This ordering, where the rheological threshold falls below the electrical threshold, is consistent with established percolation theory for polymer nanocomposites. A sparse filler network is sufficient to restrict polymer chain mobility and trigger rheological percolation, whereas electrical conductivity requires fillers to approach within approximately 5 nm of one another to enable electron tunneling or hopping. An average molecular weight for Sylgard 184 is difficult to establish due to its bimodal chain length distribution; the higher molecular weight fraction (67 000 g mol^{-1}) is therefore used here.[49] Assuming a molecular weight of 67 000 g mol^{-1} for the higher molecular weight fraction of Sylgard 184,[49] the radius of gyration was estimated using chain statistics for an unperturbed coil and hydrodynamic scaling for a swollen coil, as detailed in the SI. The unperturbed approximation yields $R_g \approx 7.08$ nm and the Flory–Fox equation yields 7.69 nm. Both estimates exceed the ~5 nm inter-particle spacing required for electron transport, such that a higher filler concentration is needed to reach the electrical percolation threshold than the rheological one. In carbon nanotube/poly(methyl methacrylate) (CNT/PMMA),[9] the critical concentration for electrical percolation is approximately three times higher than its rheological percolation. However, in the CPN/PDMS system, this difference is greater than eight times the rheological threshold.

The primary reason for the substantial difference in threshold values is that unlike conventional nanofillers that agglomerate in aqueous environments and disperse in organic solvents, CPNs are hydrophilic and disperse in aqueous solutions and can be manipulated to form various bundles in organic media,[45] thus apolar PDMS is expected to inhibit the CPNs from extending to their maximum length, thereby reducing their interaction with the polymer matrix. Fluorescence imaging (Fig. 3b) qualitatively confirmed the relative dispersion of CPNs in PDMS, however, the polarity mismatch between the filler and the matrix likely hinders the filler from forming a fully interconnected web. Beyond polarity differences, the relative flexibility of CPNs influences their interaction with the matrix in a manner distinct from more rigid CNT and AgNWs. While commercial fillers like CNT and AgNWs are stiff, rod-like structures, the shorter calculated persistence lengths of CPNs ($L_{p,CPNs}$ = 1.25 μm, see SI) suggest they are more likely to bend and curl. The calculation of persistence length is supported by the observation of type IV pili in *Pseudomonas aeruginosa*, which also has a persistence length of approximately 1 μm measured by using AFM images.[50] Additionally, electron propagation along CPNs is considered to involve hopping *via* the aromatic cores of the subunits;[51] however, the mechanisms are not yet fully understood.[32] The experimental data shown above provides converging, indirect evidence of workable dispersion for fundamental studies; however, more concerted efforts to fully develop and apply quantitative dispersion protocols for CPNs in polymeric matrices will be critical for their design and optimization as viable functional nanocomposite systems.

3.4 Enhancing CPN/PDMS conductivity *via* templating and whole cells

Recent studies have demonstrated the direct integration of bacteria into an elastomer, yielding viable, functional nano-

composites with robust ammonia-sensing capabilities.[28] To achieve higher electrical conductivity with a lower threshold, a similar "whole-cell" fabrication approach was employed, in which CPN-expressing *E. coli* cells were directly mixed into PDMS. This method simplified fabrication by eliminating purification steps (sonication, vortexing, drying, resuspension). However, distinguishing the portion of the overall filler weight percentage related to the CPNs *versus* that of the insulating cells is rather complex, so here the entire cellular filler was used instead to calculate the filler wt%. Whole-cell nanocomposites exhibited a lower percolation threshold (4.8 wt%) than those containing purified, isolated CPNs, although overall conductivity was reduced due to the insulating nature of the *E. coli* cell bodies (Fig. 5d, purple),[11] which simultaneously reduce the effective filler volume of conductive CPNs, but also likely increases the relative presence of attached CPNs and subsequent increase in CPN-to-CPN overlap frequency.

Previously, CNTs dispersed in poly(3-hexylthiophene-2,5-diyl) (P3HT) and infiltrated within AAO nanochannels showed filler alignment and enhanced electrical conductivity.[36] This precedent motivated the application of similar geometric confinement strategies *via* AAO nanochannels to the CPN/PDMS system here, which likely impose non-trivial extension forces on both the polymer chains and CPN nanofillers, thus promoting some degree of elongation and texturization of the filler relative to the randomly dispersed system. The IV curve of pristine PDMS infiltrated within the AAO template confirms the electrically insulating baseline of the unfilled template prior to CPN infiltration (Fig. S4). Infiltrating 3 wt% of CPNs within 140 nm pores resulted in conductivity values (9.9×10^{-5} S cm^{-1}; Fig. 5d, pink), comparable to the conventional, drop-cast 10 wt% CPN/PDMS system (11.1×10^{-5} S cm^{-1}; Fig. 5d, blue). Notably, a significant reduction in filler content to just 0.1 wt% yielded conductivity values beyond the electrical threshold, as shown in Fig. 5c and d. These results support the use of nanochannel arrays to potentially overcome polarity-induced aggregation and enable efficient electron transport at minimal filler loadings, facilitated by the likely formation of dense, more oriented networks within confined geometries.

Preliminary strain sensing behavior was evaluated using mm-scale, 20 wt% CPN/PDMS nanocomposite dog-bone test structures extended to 50% strain (Fig. S5a). We note that CPN synthesis at the quantities required for larger test structures is not yet a facile process, and achieving controlled dispersion at these sample volumes introduces additional complexity relative to the thin-film composites used for the percolation studies above. These constraints informed the scope of this pilot demonstration, which was designed to confirm that the composite resistance responds measurably and linearly to elongation, rather than to optimize device performance. The results confirm (i) successful scaling of CPN dispersions to 675 μg μL^{-1} while retaining functionality, and (ii) a linear resistive response across the full strain range (Fig. S5b). The gauge factor of 0.47, while below commercial benchmarks ($k \geq 2$), is consistent with an unoptimized pilot system. Stability, repeatability, and dynamic response time represent the primary

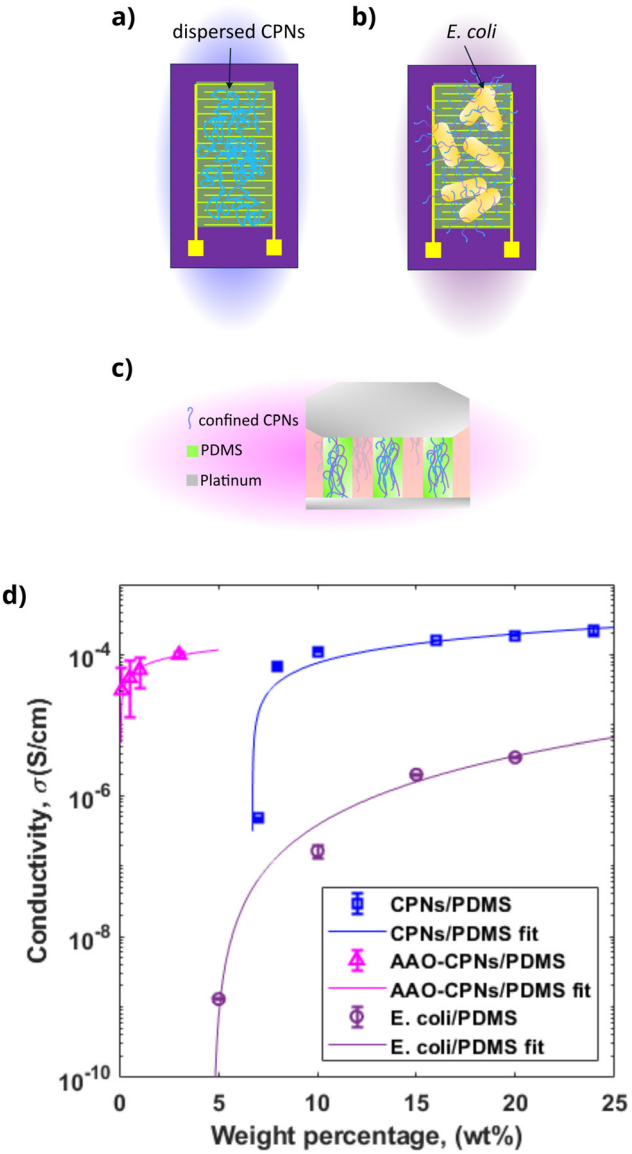

Fig. 5 (a, b and c) show the schematic diagrams of CPN/PDMS *I–V* tests, *E. coli*/PDMS *I–V* tests, and anodic aluminum oxide template fabrication for *I–V* tests, respectively. (d) Shows the electrical percolation of CPN/PDMS (blue), *E. coli*/PDMS (violet) and AAO-CPN/PDMS (pink). The *E. coli*/PDMS fit yields $w_{cr,\sigma}$ = 4.8 wt% (R^2 = 0.83), trading a slight reduction in threshold percentage for a two orders of magnitude reduction in conductivity. The AAO-CPN/PDMS fit yields a $w_{cr,\sigma}$ = 0.1 wt% (R^2 = 0.98), a drastic reduction in electrical threshold despite similar conductivity as dispersed, isolated CPN/PDMS.

targets of subsequent sensor-focused work, which will build on the structural and dispersion approaches established here to engineer reductions in percolation threshold and improve composite performance at scale.

4. Conclusions

In conclusion, CPNs were dispersed within PDMS to successfully fabricate a polymer nanocomposite system that dis-

plays classic rheological and electrical percolation threshold behavior. Using scanning probe nanomechanics methods, the first experimental elastic modulus of individual CPNs (1.3 ± 0.1 GPa) was established, validating their potential as compliant components for soft electronics. Additionally, tunable mechanical ($w_{cr,E}$ = 0.8 wt%) and electrical ($w_{cr,\sigma}$ = 6.7 wt%) percolation behavior was observed in the CPN/PDMS nanocomposites. While the polarity mismatch between the CPNs and PDMS matrix presents challenges for random dispersion, a demonstration of structural templating *via* AAO successfully reduced the electrical percolation threshold by two orders of magnitude ($w_{cr,\sigma}$ = 0.1 wt%). These findings, coupled with a facile "whole-cell" ($w_{cr,\sigma}$ = 4.8 wt%) fabrication route, expand the toolkit for designing sustainable, bio-based electronic materials based on bulk CPN/PDMS structures for advanced applications in soft electronics.

Author contributions

E. C. led all nanocomposite fabrication, nanomechanics measurements, transport measurements, percolation analyses and writing. J. M. S. led CPN synthesis protocols. T. L. W. performed electron microscopy imaging and analysis. M.-C. C. led CPN functionalization, fluorescence microscopy and analysis. J. D. S. supervised general nanocomposite fluorescence studies, overall analysis and technical writing. S. S. N. conceptualized and led the overall project administration, scope, experimental plan, analysis, and writing.

Conflicts of interest

The authors declare that they have no known competing financial interests or personal relationships that could have appeared to influence the work reported in this paper.

Data availability

The raw data supporting this article are available at figshare at doi: https://doi.org/10.6084/m9.figshare.31605181.

Supplementary information (SI) is available. The supplementary information includes persistence length calculations for CPNs, CNTs, and AgNWs; AFM height and modulus line profiles for individual CPNs; AM-FM bimodal modulus maps as a function of filler loading; representative *I–V* curves above and below the electrical percolation threshold; the radius of gyration estimation for Sylgard 184 PDMS chains; the baseline *I–V*curve for pristine PDMS-infiltrated AAO templates; and strain sensing pilot data for CPN/PDMS dog-bone test structures. See DOI: https://doi.org/10.1039/d6lp00122j.

Acknowledgements

The authors thank Prof. Derek R. Lovley for useful discussions related to CPN preparation and analysis. S. S. N., J. D. S., and E. C. acknowledge the support from the National Science Foundation, NSF-DMREF 1921839. J. D. S. acknowledges the support of the Gary R. Lapidus Fellowship. J. M. S. acknowledges support from the Fulbright–Nehru Postdoctoral Fellowship. Electron microscopy images were obtained at the University of Massachusetts Electron Microscopy Core Facility, RRID: SCR_027853.

References

1 R. M. Erb, K. H. Cherenack, R. E. Stahel, R. Libanori, T. Kinkeldei, N. Münzenrieder, G. Tröster and A. R. Studart, *ACS Appl. Mater. Interfaces*, 2012, **4**, 2860–2864.
2 M. D. Bartlett, E. J. Markvicka and C. Majidi, *Adv. Funct. Mater.*, 2016, **26**, 8496–8504.
3 C. Wang, C. Wang, Z. Huang and S. Xu, *Adv. Mater.*, 2018, **30**, 1801368.
4 A. Chortos, J. Liu and Z. Bao, *Nat. Mater.*, 2016, **15**, 937–950.
5 D.-H. Kim, J. Viventi, J. J. Amsden, J. Xiao, L. Vigeland, Y.-S. Kim, J. A. Blanco, B. Panilaitis, E. S. Frechette, D. Contreras, D. L. Kaplan, F. G. Omenetto, Y. Huang, K.-C. Hwang, M. R. Zakin, B. Litt and J. A. Rogers, *Nat. Mater.*, 2010, **9**, 511–517.
6 K.-J. Cho, J.-S. Koh, S. Kim, W.-S. Chu, Y. Hong and S.-H. Ahn, *Int. J. Precis. Eng. Manuf.*, 2009, **10**, 171–181.
7 G. Reguera, K. D. McCarthy, T. Mehta, J. S. Nicoll, M. T. Tuominen and D. R. Lovley, *Nature*, 2005, **435**, 1098–1101.
8 S. K. Kumar, B. C. Benicewicz, R. A. Vaia and K. I. Winey, *Macromolecules*, 2017, **50**, 714–731.
9 F. Du, R. C. Scogna, W. Zhou, S. Brand, J. E. Fischer and K. I. Winey, *Macromolecules*, 2004, **37**, 9048–9055.
10 S. I. White, R. M. Mutiso, P. M. Vora, D. Jahnke, S. Hsu, J. M. Kikkawa, J. Li, J. E. Fischer and K. I. Winey, *Adv. Funct. Mater.*, 2010, **20**, 2709–2716.
11 N. S. Malvankar, M. Vargas, K. P. Nevin, A. E. Franks, C. Leang, B.-C. Kim, K. Inoue, T. Mester, S. F. Covalla, J. P. Johnson, V. M. Rotello, M. T. Tuominen and D. R. Lovley, *Nat. Nanotechnol.*, 2011, **6**, 573–579.
12 J.-B. Lee and D.-Y. Khang, *Compos. Sci. Technol.*, 2012, **72**, 1257–1263.
13 F. Xu and Y. Zhu, *Adv. Mater.*, 2012, **24**, 5117–5122.
14 Y. Chen, Z. Ouyang, M. Gu and W. Cheng, *Adv. Mater.*, 2013, **25**, 80–85.
15 S. Gong, W. Schwalb, Y. Wang, Y. Chen, Y. Tang, J. Si, B. Shirinzadeh and W. Cheng, *Nat. Commun.*, 2014, **5**, 3132.
16 S. Han, S. Hong, J. Ham, J. Yeo, J. Lee, B. Kang, P. Lee, J. Kwon, S. S. Lee, M.-Y. Yang and S. H. Ko, *Adv. Mater.*, 2014, **26**, 5808–5814.

17 S. Yao and Y. Zhu, *Nanoscale*, 2014, **6**, 2345–2352.
18 F. Mattarozzi, N. van der Willige, V. Gulino, C. Keijzer, R. C. J. van de Poll, E. J. M. Hensen, P. Ngene and P. E. de Jongh, *ChemCatChem*, 2023, **15**, e202300792.
19 R. J. Chimentão, I. Kirm, F. Medina, X. Rodríguez, Y. Cesteros, P. Salagre, J. E. Sueiras and J. L. G. Fierro, *Appl. Surf. Sci.*, 2005, **252**, 793–800.
20 T. Lim, M. Kim, A. Akbarian, J. Kim, P. A. Tresco and H. Zhang, *Adv. Healthcare Mater.*, 2022, **11**, 2102382.
21 M. D. Dickey, *Adv. Mater.*, 2017, **29**, 1606425.
22 A. Koh, J. Sietins, G. Slipher and R. Mrozek, *J. Mater. Res.*, 2018, **33**, 2443–2453.
23 Y. Tan, R. Y. Adhikari, N. S. Malvankar, J. E. Ward, T. L. Woodard, K. P. Nevin and D. R. Lovley, *mBio*, 2017, **8**, e02203-16, DOI: 10.1128/mbio.02203-16.
24 D. J. F. Walker, E. Martz, D. E. Holmes, Z. Zhou, S. S. Nonnenmann and D. R. Lovley, *The Archaellum of Methanospirillum hungatei is Electrically Conductive*, 2018, https://www.biorxiv.org/content/10.1101/458356v1, Pages: 458356 Section: New Results.
25 D. J. Walker, R. Y. Adhikari, D. E. Holmes, J. E. Ward, T. L. Woodard, K. P. Nevin and D. R. Lovley, *ISME J.*, 2018, **12**, 48–58.
26 D. J. F. Walker, K. P. Nevin, D. E. Holmes, A.-E. Rotaru, J. E. Ward, T. L. Woodard, J. Zhu, T. Ueki, S. S. Nonnenmann, M. J. McInerney and D. R. Lovley, *Syntrophus Conductive Pili Demonstrate that Common Hydrogen-Donating Syntrophs can have a Direct Electron Transfer Option*, 2018, https://www.biorxiv.org/content/10.1101/479683v1, Pages: 479683 Section: New Results.
27 T. Fu, X. Liu, H. Gao, J. E. Ward, X. Liu, B. Yin, Z. Wang, Y. Zhuo, D. J. F. Walker, J. J. Yang, J. Chen, D. R. Lovley and J. Yao, *Nat. Commun.*, 2020, **11**, 1861.
28 J. M. Sonawane, E. Chia, T. Ueki, T. Woodard, J. Greener, S. S. Nonnenmann, J. Yao and D. R. Lovley, *Biosens. Bioelectron.*, 2025, **278**, 117378.
29 X. Liu, H. Gao, J. E. Ward, X. Liu, B. Yin, T. Fu, J. Chen, D. R. Lovley and J. Yao, *Nature*, 2020, **578**, 550–554.
30 E. Bullitt and L. Makowski, *Biophys. J.*, 1998, **74**, 623–632.
31 X. Zhao, Y. Liu, Z. Guo, Y. Zhang, Y. Li and W. Liu, *J. Biomech.*, 2017, **56**, 97–101.
32 Y.-L. Sun, H.-Y. Tang, A. Ribbe, V. Duzhko, T. L. Woodard, J. E. Ward, Y. Bai, K. P. Nevin, S. S. Nonnenmann, T. Russell, T. Emrick and D. R. Lovley, *Small*, 2018, **14**, 1802624.
33 T. Ueki, D. J. F. Walker, T. L. Woodard, K. P. Nevin, S. S. Nonnenmann and D. R. Lovley, *ACS Synth. Biol.*, 2020, **9**, 647–654.
34 Y. Lekbach, T. Ueki, X. Liu, T. Woodard, J. Yao and D. R. Lovley, *Biosens. Bioelectron.*, 2023, **226**, 115147.
35 A. Labuda, S. Hohlbauch, M. Kocun, F. T. Limpoco, N. Kirchhofer, B. Ohler and D. Hurley, *Micros. Today*, 2018, **26**, 12–17.
36 M. K. Smith, V. Singh, K. Kalaitzidou and B. A. Cola, *ACS Appl. Mater. Interfaces*, 2016, **8**, 14788–14794.
37 R. Garcia and J. R. Tejedor, *Nanoscale Adv.*, 2025, **7**, 6286–6307.
38 G. Zhou, B. Zhang, G. Tang, X.-F. Yu and M. Galluzzi, *Adv. Phys.:X*, 2021, **6**, 1866668.
39 J. Wang, J.-Q. Han, Y. Yan, M.-N. Yu, Q.-Y. Feng and L.-H. Xie, *ACS Appl. Mater. Interfaces*, 2025, **17**, 55689–55705.
40 M. L. Oyen, *Philos. Mag.*, 2006, **86**, 5625–5641.
41 M. M. J. Treacy, T. W. Ebbesen and J. M. Gibson, *Nature*, 1996, **381**, 678–680.
42 Y. Chen, B. L. Dorgan, Jr., D. N. McIlroy and D. Eric Aston, *J. Appl. Phys.*, 2006, **100**, 104301.
43 X. Liu, D. J. F. Walker, S. S. Nonnenmann, D. Sun and D. R. Lovley, *mBio*, 2021, **12**, DOI: 10.1128/mbio.02209–21.
44 M. Kocun, A. Labuda, W. Meinhold, I. Revenko and R. Proksch, *ACS Nano*, 2017, **11**, 10097–10105.
45 Y.-L. Sun, B. J. Montz, R. Selhorst, H.-Y. Tang, J. Zhu, K. P. Nevin, T. L. Woodard, A. E. Ribbe, T. P. Russell, S. S. Nonnenmann, D. R. Lovley and T. Emrick, *Biomacromolecules*, 2021, **22**, 1305–1311.
46 D.-K. Lee, J. Yoo, H. Kim, B.-H. Kang and S.-H. Park, *Materials*, 2022, **15**, 1356.
47 D. Ao, Y. Tang, X. Xu, X. Xiang, J. Yu, S. Li and X. Zu, *Nanomaterials*, 2020, **10**, 768.
48 W. Bauhofer and J. Z. Kovacs, *Compos. Sci. Technol.*, 2009, **69**, 1486–1498.
49 N. Stafie, D. Stamatialis and M. Wessling, *Sep. Purif. Technol.*, 2005, **45**, 220–231.
50 S. Lu, A. Touhami, H. Harvey, E. Scheurwater, L. Burrows and J. R. Dutcher, *Biophys. J.*, 2009, **96**, 641a–642a.
51 D. R. Lovley, *Curr. Opin. Electrochem.*, 2017, **4**, 190–198.